Journal of
Mechanics of Materials and Structures

A MACROSCOPIC MODEL FOR KINK BANDING INSTABILITIES IN FIBER COMPOSITES

Shiladitya Basu, Anthony M. Waas and Damodar R. Ambur

Volume 1, Nº 6 *June 2006*

mathematical sciences publishers

JOURNAL OF MECHANICS OF MATERIALS AND STRUCTURES
Vol. 1, No. 6, 2006

A MACROSCOPIC MODEL FOR KINK BANDING INSTABILITIES IN FIBER COMPOSITES

SHILADITYA BASU, ANTHONY M. WAAS AND DAMODAR R. AMBUR

In this paper, a mechanism-based lamina level modeling approach is used as the basis for developing a macroscopic (lamina level) model to capture the mechanisms of kink banding. Laminae are modeled as inelastic degrading *homogenized* layers in a state of plane stress according to Schapery Theory (ST). However, the principal orthotropic material axes are allowed to rotate as a function of deformation. In ST, each lamina degrades as characterized through laboratory scale experiments. In the fiber direction, elastic behavior prevails; however, in this work, the phenomenon of fiber microbuckling leading to kink banding, which is responsible for the sudden degradation of the axial lamina properties under compression, is explicitly accounted for by allowing the fiber rotation at a material point to be a variable in the problem. These features are built into a user-defined material subroutine that is implemented through the commercial finite element (FE) software ABAQUS. Thus, in this model we eschew the notion of a fixed compressive strength of a lamina and instead use the mechanics of the failure process to provide the in situ compression strength of a material point in a lamina, the latter being dictated strongly by the current local stress state, the current state of the lamina transverse material properties, and the local fiber rotation. The inputs to this model are laboratory scale, coupon level test data (at the lamina level) that provide information on the lamina transverse property degradation (that is, appropriate, measured, strain-stress relations of the lamina transverse properties), the elastic lamina orthotropic properties and the geometry of the lamina. The validity of the approach advocated is demonstrated through numerical simulations of unidirectional lamina with initial fiber imperfections. The predictions of the simulations reported in this paper are compared against previously reported results from micromechanical analyses. Good agreement between the present macroscopic modeling approach and the previous micromechanical observations are reported.

1. Introduction

Development of computational methodologies for the prediction of damage accumulation and growth in continuous fiber composite laminates is an active area of research. There exists a large body of literature devoted to progressive failure analysis (PFA) of composite laminated structures. Many of the PFA schemes available today rely on the phenomenological approach of defining strength criteria for a single lamina when subjected to different single component stress states. These methods define the onset of failure through specific indices that are expressed as functions of the current stress state. When any of these indices exceeds a predefined critical value, the material at that point is said to have failed [Hashin 1980; Chang and Lessard 1991]. When a material point has failed, for subsequent loading, it is assumed to have a reduced stiffness that is predetermined in an empirical manner. Depending on the type of failure (for instance, fiber breaking and/or matrix cracking due to tension along the fibers, fiber kink-banding due

Keywords: fiber kinking, fiber rotation, matrix damage, progressive failure analysis, compressive response.

to compression along the fibers, fiber/matrix debonding due to in-plane shear), different elastic moduli are set to zero. In addition, linear elastic material behavior is assumed throughout the analysis.

In a laminated composite plate, the stiffness at a material point is determined by the current local stress state and the local 'state' of the material. The local stress state, in general, is multiaxial and a material point at the current state may have accumulated damage, dictated by the loading history. Thus, 'strength' at a material point is influenced to a great extent by the current stress and strain state and is predicated on the mechanism of failure. PFA methodologies that abruptly change material properties based on strength 'indices' and rely on a linear elastic analysis may be unable to realistically account for features associated with the mechanisms of failure. Furthermore, these approaches lack an appropriate definition of the material state beyond first failure. For progressive failure modeling, a framework that accounts for the continued degradation of the material is needed.

Schapery [1990] introduced a thermodynamically based theory (referred to as ST) that uses internal state variables (ISVs) to analyze damage evolution in composite laminates. These ISVs are related to mechanical aspects of damage mechanisms. The ISVs are related to the energy required for the evolution of the damaged states. Different damage mechanisms can have distinct ISVs to track the damage evolution. For instance, matrix microcracking can be expressed via one ISV, while transverse cracking can be represented by another ISV [Schapery and Sicking 1995]. The evolution of these ISVs with global loading is determined at each material point as functions of load history, by means of a thermodynamic criterion (an evolution equation) throughout the loading history. Therefore, the 'state' of the material is continually updated according to the stress and strain history that a material point experiences throughout the loading history.

Various experimental [Vogler and Kyriakides 1999; Lee and Waas 1999; Oguni et al. 2000] and analytical [Basu et al. 2006a] studies show that the maximum load sustained by a lamina in the axial direction (σ_{11}^{cr}) in compression depends greatly on the presence of other in-plane stress components such as σ_{22} and τ_{12}. Experimental, analytical and micromechanical studies show that the main physical event occurring during kink banding is the rotation of fibers in a band within a degrading matrix. The rotation of fibers gives rise to high localized shear strains that drive the shear degradation of the local matrix. The shear degradation in turn drives the rotation of the fibers creating a positive feedback loop. These simultaneous phenomena result in a limit load situation for a lamina under axial compression. This limit load, which is dictated by the local stress state and the state of the transverse lamina properties, can be relieved (increased) by the presence of other stress components or, in certain cases, can be elevated (reduced). The present approach captures these two phenomena in a macroscopic numerical setting and is able to reproduce the fine scale micromechanical observations seen in experiments and in associated numerical models [Vogler and Kyriakides 1997; Lee and Waas 1999; Yerramalli and Waas 2004; Basu 2005; Basu et al. 2006b]. It is to be noted that Merodio and Pence [2001] have presented a comprehensive analysis of the formation of kinks, defined as surfaces across which the deformation gradient and hydrostatic pressure suffer jumps, in directionally reinforced neo-Hookean materials. Their results, which are carried out for purely elastic materials, bear some resemblance to the results reported in the literature for fiber reinforced materials with a polymer matrix [Vogler and Kyriakides 1997; Lee and Waas 1999; Oguni et al. 2000]. This work has recently been further extended by Fu and Zhang [2006], who have considered the rotation of the kink band with continued loading.

2. Modeling of a damaging matrix using Schapery Theory (ST)

2.1. *Elements of the PFA approach.*

2.1.1. *Non-linear constitutive formulation.* Schapery [1989] developed nonlinear elastic constitutive relations for an orthotropic lamina using a work potential approach which accounted for the effect of microdamage. The lamina stress-strain relations are

$$\sigma_{11} = Q_{11}\epsilon_{11} + Q_{12}\epsilon_{22}, \qquad \sigma_{22} = Q_{12}\epsilon_{11} + Q_{22}\epsilon_{22}, \qquad \tau_{12} = Q_{66}\gamma_{12}, \tag{1}$$

where

$$Q_{11} = \frac{E_{11}}{1 - \nu_{12}\nu_{21}}, \quad Q_{22} = \frac{E_{22}}{1 - \nu_{12}\nu_{21}},$$
$$Q_{12} = \nu_{12}Q_{22}, \quad Q_{66} = G_{12},$$
$$\nu_{21} = \frac{\nu_{12}E_{22}}{E_{11}}$$

In the existing literature on damage mechanics as applied to continuous fiber laminated composite materials, the effect of damage is incorporated through the change in transverse Young's modulus E_{22} and in plane shear modulus G_{12}. For instance, Sun and Chen [1989] proposed a one parameter plastic potential in conjunction with orthotropic incremental plasticity theory to study the evolution of E_{22} and G_{12} in tension. Schapery and Sicking [1995] used ST to study the evolution of E_{22} and G_{12}. These studies were not concerned with the state of the lamina beyond first failure in the fiber direction. Yet it is recognized [Dávila et al. 2000] that such damage is dominant for compression loaded composite structures. Lamina level coupon tests in tension have shown that fiber direction modulus E_{11} and Poisson's ratio ν_{12} can be assumed to be independent of microdamage that influences E_{22} and G_{12} [Schapery 1995]. This is also true for compression until the onset of kinking (the axial compression load reaches a maximum limit load at the point in which a kink band starts to form, for example, as shown in [Lee and Waas 1999]). During kink band formation and propagation, it is likely that microdamage mechanisms do influence E_{11}, ν_{12}, E_{22} and G_{12}. Subsequent to kink banding, other failure mechanisms such as delamination can occur. These mechanisms are not accounted for here, but have received attention recently in the context of PFA [Goyal et al. 2002].

2.1.2. *Elements of Schapery Theory.* Schapery [1990] introduced a general thermodynamic framework to study materials that undergo damage. In [Schapery and Sicking 1995], ISVs are used to incorporate *inelastic* behavior in the material response. In these developments in a mechanical process the total work done, W_T, is composed of the inelastic work, W_s and the work of deformation W: $W_T = W + W_s$. The irrecoverable portion of total energy (W_s) can be determined from the material stress-strain response as shown in Figure 1. ISVs are described through S_i's. Each S_i is associated with a particular damage mechanism. To satisfy the path independence of total work, these ISVs have to satisfy the following relation,

$$f_i = \frac{\partial W_s}{\partial S_i}. \tag{2}$$

The left-hand side of Equation (2) is called the *thermodynamic force* related to the i^{th} ISV. If the i^{th} *driving force*, which is the available thermodynamic force, given by Equation (3), exceeds $\partial W_s/\partial S_i$,

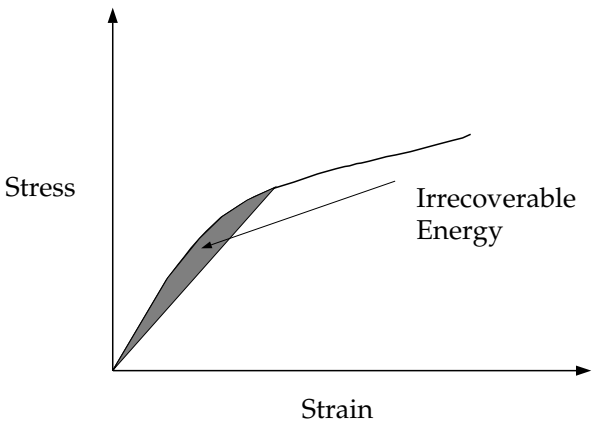

Figure 1. Definition of irrecoverable energy using a generic stress-strain curve.

then the material undergoes a structural change associated with S_i:

$$f_i \equiv -\frac{\partial W}{\partial S_i}. \tag{3}$$

Stated another way, $\dot{S}_i > 0$. However, as Schapery [1990] pointed out, if the available thermodynamic force $(-\partial W/\partial S_i)$ is less than the required thermodynamic force $(\partial W_s/\partial S_i)$, then $\dot{S}_i = 0$. Furthermore, S_i need not change continuously with the loading.

Schapery considered two ISVs. They were the energies associated with matrix microcracks (S) and of the transverse intra-ply cracks (S_c), respectively. Inelastic work is described as $W_s = S + S_c$. In the present work, the effect of only one ISV is considered; it is denoted by S and represents the irrecoverable energy content due to the accumulation of microcracks.

The ISV affects the moduli E_{22} and G_{12} through Equation (4):

$$E_{22} = E_{22_0} e_s(S), \qquad G_{12} = G_{12_0} g_s(S). \tag{4}$$

Here, E_{22_0} and G_{12_0} are transverse and shear moduli of the virgin material, that is, at zero strain and zero damage; $e_s(S)$ and $g_s(S)$ are functions relating these two moduli to microcracking ISV, S. The functions e_s and g_s are expressed as polynomial relations in the ISV, S [Schapery and Sicking 1995].

The strain energy density (or work of deformation) can be written as

$$W = \tfrac{1}{2}\left(Q_{11}\epsilon_{11}^2 + Q_{22}\epsilon_{22}^2\right) + Q_{12}\epsilon_{11}\epsilon_{22} + \tfrac{1}{2}Q_{66}\gamma_{12}^2. \tag{5}$$

To incorporate geometric nonlinearities, Green's strains and the second Piola Kirchoff stresses need to be used in the expression for W. For small strains, Equation (5) would contain only the first order terms in the strain-displacement relations. Schapery and Sicking [1995] have shown that material nonlinearities as incorporated in Equation (5) are still significant for fiber reinforced composites even when inclusion of geometric nonlinearities are not called for [Schapery 2002]. Using Equations (1)–(3), the evolution

equation for S is as follows,

$$\frac{\epsilon_{11}^2}{2}\frac{\partial Q_{11}}{\partial S}+\frac{\epsilon_{22}^2}{2}\frac{\partial Q_{22}}{\partial S}+\epsilon_{11}\epsilon_{22}\frac{\partial Q_{12}}{\partial S}+\frac{\gamma_{12}^2}{2}\frac{\partial G_{12}}{\partial S}=-1. \tag{6}$$

For most materials, $\nu_{12}\nu_{21}\ll 1$, which implies that the Q_{ij}'s can be replaced by E_{ij}'s. In this work, it is assumed that the fiber direction stiffnesses are unaffected by S. Thus, the term containing Q_{11} in Equation (6) can be neglected. It is also assumed that ν_{12} changes with S such that $\nu_{12}E_{22}$ remains constant during loading. The implications of this assumption are twofold. Firstly, it allows for a change in ν_{12} with damage accumulation in the lamina. Secondly, it makes it possible to uncouple ϵ_{11} from the microcracking damage accumulation. If ϵ_{11} is present in the evolution equation (Equation (6)), then microcracking damage becomes a direct function of the longitudinal strain, which is an improper representation of the underlying mechanism. Equation (6) can be reduced to

$$\frac{\epsilon_{22}^2}{2}\frac{\partial E_{22}}{\partial S}+\frac{\gamma_{12}^2}{2}\frac{\partial G_{12}}{\partial S}=-1.$$

For an inelastic process, the entropy production rate is nonnegative. Hence,

$$\dot{S}\geq 0. \tag{7}$$

The overdot represents temporal derivative. Physically, $\dot{S}$ is nonnegative because healing (or reversible damage) is not allowed for in the damage mechanism considered.

From experiments [Schapery and Sicking 1995], it has been observed that for small strains, S behaves as ϵ^3. This is based on the fact that the moduli are constant for small strains. Thus to express the moduli E_{22} and G_{12} in terms of a polynomial of S, a reduced variable S_r can be used, namely, $S_r\equiv S^{1/3}$. The evolution equation for S_r now becomes

$$\frac{\epsilon_{22}^2}{2}\frac{\partial E_{22}}{\partial S_r}+\frac{\gamma_{12}^2}{2}\frac{\partial G_{12}}{\partial S_r}=-3S_r^2. \tag{8}$$

It should be noted that it is possible to include other softening damage mechanisms such as local fiber-matrix debonding and shear banding through S as has been discussed by Schapery [1990].

During laboratory experiments, the density of microcracks in a lamina reaches a saturation limit and the specimen fails in a catastrophic manner. The corresponding value of S_r, obtained from the resultant stress-strain plot, is denoted by S_r^*. The constitutive model described thus far holds true for $S_r\leq S_r^*$. For $S_r>S_r^*$, any constitutive modeling idea is somewhat hypothetical as no material physically exists anymore. For the purpose of extending the analyses beyond S_r^*, it is imperative for the design of a PFA to ensure a stable procedure to degrade the material beyond this point.

2.1.3. *Fiber rotation under axial compression.* Imperfect fiber systems are prone to rotation under axial compression. That is, the fibers within a lamina that are subjected to axial compression have the propensity to *change* their alignment. This change is dictated by the local multiaxial stress state and the local shear stiffness of the matrix. As the local shear strains increase, the matrix shear stiffness decreases, which indicates that the resistance to fiber rotation diminishes and gradually the fiber rotation begins to build up, which in turn creates more local imperfection and local shear strain. Thus, a positive feedback loop is established between these two competing events. A point is reached when the in situ shear stiffness

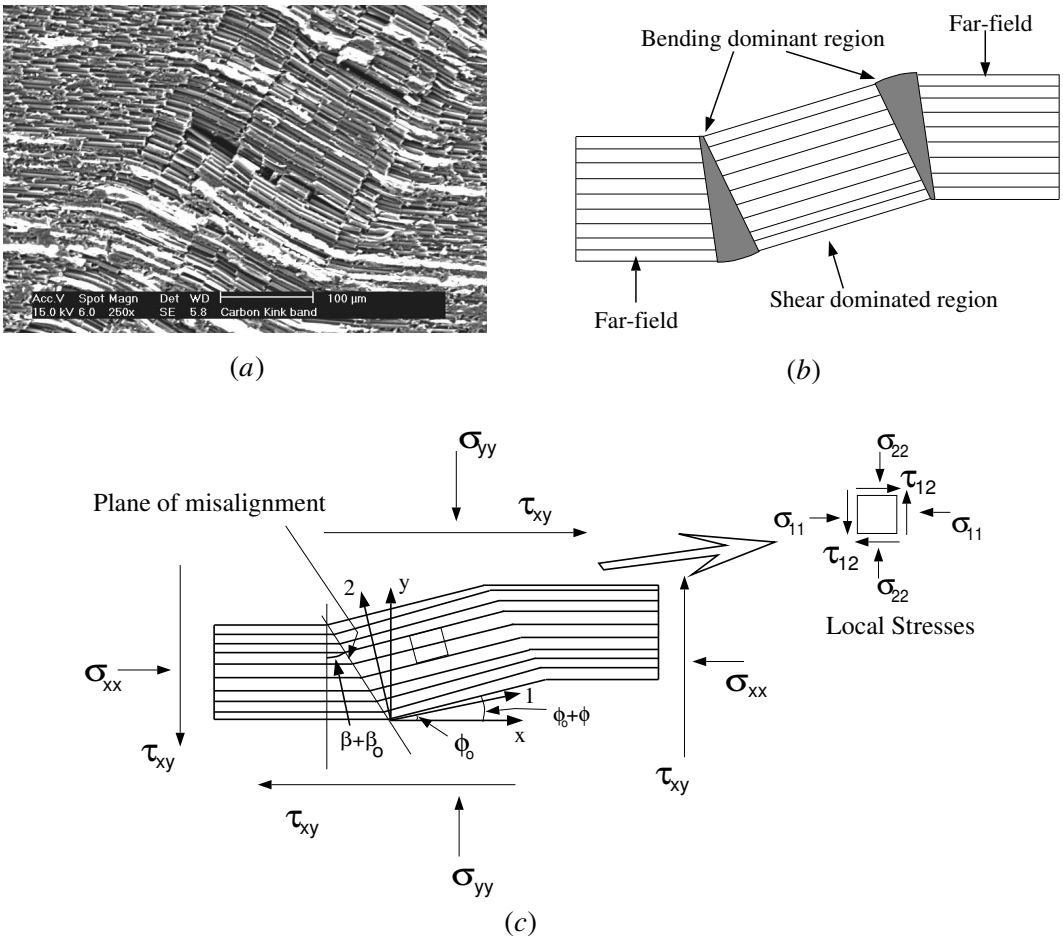

Figure 2. (a) The developing kink band in Carbon composites [Yerramalli 2003]; (b) the schematic representation of such within a lamina; and (c) a unidirectional lamina with a band of misaligned fibers in equilibrium under a multiaxial stress state. Inset shows the stress state inside the misaligned band.

is *not* sufficient to prevent additional fiber rotation. This point usually coincides with the peak load in an axial material response curve. Beyond this point, the matrix offers diminishing resistance to fiber rotation and the fibers rotate and break along boundaries within localized deformed bands, commonly described as 'kink bands' [Evans and Adler 1978].

Consider a fiber reinforced lamina under a generalized load state as indicated in Figure 2. A reference frame x–y can be defined such that the x-direction is parallel to the nominal fiber direction in the lamina and the y-direction is normal to it. In subsequent discussions, the x–y reference frame will be termed as the 'global' frame. The misaligned band of fibers, in the current configuration, is defined through two angles, $\hat{\phi} = \phi + \phi_0$ and $\hat{\beta} = \beta + \beta_0$. The angles ϕ_0 and β_0 are constants, and the angles ϕ and β are variables that may change as a function of current far-field stress state. The reference frame 1–2 is defined in the unstressed initial configuration of the misaligned lamina. Fibers inside the misaligned band

are parallel to the '1' direction in the initial state. A current reference frame $1'$–$2'$ is defined where '$1'$' is always parallel to the current fiber direction inside the band, so that the 1-axis rotates to $1'$-axis during loading. The '2' and '$2'$' directions are always orthogonal to the '1' and '$1'$' directions respectively. The 1–2 frame will be defined as the 'local' frame and the $1'$–$2'$ system will be termed the instantaneous frame. Initially, when the matrix retains most of its in situ shear stiffness, the 1–2 and $1'$–$2'$ axes systems will be nearly coincident. As the matrix loses its in situ shear stiffness, the local shear strain, γ_{12}, will start to rise rapidly. As shown in Basu et al. [2006a], the angle between the 1-axis and the $1'$-axis, given by ϕ and γ_{12}, for small strains, is related by $\gamma_{12} = \gamma_{12}^{\infty} + \phi - \beta$. Here, γ_{12}^{∞} is the contribution from the externally applied shear loading, if any. For a uniaxial compression loading and assuming $\beta = \beta_0 = 0$, we arrive at

$$\gamma_{12} \approx \phi. \tag{9}$$

2.1.4. *Fiber rotation under axial compression-finite deformation.* In Equation (9) the angle ϕ is computed with a small strain assumption and without contribution from the fiber axial strain. In situ fiber orientation can also be computed using the deformation gradient in the following manner [Fung and Tong 2001]. If the unit vector of a line element in the undeformed configuration is given by e_{f_0}, and F is the deformation gradient tensor, then the stretch ratio of that line element due to deformation can be computed as

$$\lambda = \sqrt{e_{f_0} \cdot F^T \cdot F \cdot e_{f_0}}.$$

Consequently, the new unit vector of that line element after deformation will be

$$e_f = \frac{1}{\lambda} F \cdot e_{f_0}. \tag{10}$$

Equation (10) can be used to obtain the instantaneous fiber orientation in the 1–2 plane.

$$\phi = \arctan \frac{e_f(2)}{e_f(1)}. \tag{11}$$

This expression of ϕ is not subject to simplifications associated with the smallness of quantities.

2.2. ***Numerical implementation using the finite element (FE) method.*** The material behavior outlined in the previous subsection is modeled in the numerical domain using the commercially available FE package ABAQUS. ABAQUS has the capability of integrating user-defined material behavior with its existing element library through user-defined material subroutines, UMAT [ABAQUS 2003]. This subroutine is called at each material point for which the constitutive law is defined through the user-defined option. A UMAT receives, from the solver in ABAQUS, the stresses and strains from the previous loading step, the increment of strain in the current loading step and various other parameters. After calculations, the UMAT returns to the solver the updated stresses and internal state variables, if any, and the incremental tangent stiffness matrix, $\partial\sigma_{ij}/\partial\epsilon_{ij}$. Here it is pertinent to relate the three reference frames described in the previous subsection to the finite element solver reference systems. The x–y reference frame is the 'global' or 'laminate' frame. The master geometry of the numerical domain is defined in this system. We will also use this frame to define external loading. The 1–2 reference frame coincides with the 'local' lamina orientation, without any loss in its significance. The solver in ABAQUS passes variables to a

UMAT in this coordinate frame. The $1'$–$2'$ reference frame is the 'instantaneous' frame, with the $1'$ direction coincident with the current fiber direction, and is used for computations within the UMAT.

In the n^{th} loading increment, the solver sends in the stresses σ_{ij}^{n-1} in the 1–2 coordinate frame which are related to the stresses in the x–y frame via the plane-stress transformation relation:

$$\begin{aligned}
\sigma_{11}^{n-1} &= \cos^2(\phi^{n-1})\sigma_{xx}^{n-1} + \sin^2(\phi^{n-1})\sigma_{yy}^{n-1} + 2\cos(\phi^{n-1})\sin(\phi^{n-1})\tau_{xy}^{n-1},\\
\sigma_{22}^{n-1} &= \sin^2(\phi^{n-1})\sigma_{xx}^{n-1} + \cos^2(\phi^{n-1})\sigma_{yy}^{n-1} - 2\cos(\phi^{n-1})\sin(\phi^{n-1})\tau_{xy}^{n-1},\\
\tau_{12}^{n-1} &= \cos(\phi^{n-1})\sin(\phi^{n-1})\left(\sigma_{xx}^{n-1} - \sigma_{yy}^{n-1}\right) + \left(\cos^2(\phi^{n-1}) - \sin^2(\phi^{n-1})\right)\tau_{xy}^{n-1}.
\end{aligned}$$

The strains ϵ_{ij}^{n-1} and strain increments $\mathrm{d}\epsilon_{ij}^{n}$ in the local 1–2 coordinate system are also passed in from the solver. Within the UMAT, these local strain increments ($\mathrm{d}\epsilon_{ij}^{n}$) are added to the total strains, ϵ_{ij}^{n-1}, to obtain the total strains ϵ_{ij}^{n}. The strains, ϵ_{ij}^{n}, are then transformed to the $1'$–$2'$ system using the angle between the local and the instantaneous frames, ϕ^{n-1}, to obtain total strains in the instantaneous direction, $\epsilon_{i'j'}^{n}$. If the stored value of S_r (solution from the previous load increment) is greater than S_r^*, all material parameters are degraded in a pre-determined fashion such that a zero secant stiffness state is reached asymptotically. If $S_r < S_r^*$, then these strains $\epsilon_{i'j'}^{n}$ are used in Equation (8) to solve for the thermodynamic damage variable S_r. If the S_r value thus obtained satisfies Equation (7), then the material point accumulates damage and the lamina in situ moduli E_{22} and G_{12} are degraded according to the input data provided. If S_r does not satisfy Equation (7), then the in situ moduli are not changed from their previous values. This ensures that a material point accumulates damage without reversibility and the moduli always degrade monotonically. Subsequently, the material secant constitutive matrix $Q_{i'j'}^{n}$ is computed using the in situ moduli, E_{11}, ν_{12}, E_{22} and G_{12}. According to the present modeling scheme, E_{11} is not affected by S_r. Thus it remains constant at the undamaged state value until S_r becomes greater than S_r^* during the analysis. Next, the stresses $\sigma_{i'j'}^{n}$ are updated and the material incremental constitutive matrix $\partial\sigma_{i'j'}/\partial\epsilon_{i'j'}$ is computed:

$$J = \begin{pmatrix} E_{110} & \nu_{12}E_{22} & 0 \\ \nu_{12}E_{22} & E_{22} + \frac{\partial E_{22}}{\partial \epsilon_{22}}\epsilon_{22} & \frac{\partial E_{22}}{\partial \gamma_{12}}\epsilon_{22} \\ 0 & \frac{\partial G_{12}}{\partial \epsilon_{22}}\gamma_{12} & G_{12} + \frac{\partial G_{12}}{\partial \gamma_{12}}\gamma_{12} \end{pmatrix}$$

When the increment of shear strain is small, the instantaneous fiber rotation can be equated to the change in shear strain $\mathrm{d}\gamma_{1'2'}^{n}$ [Schapery 1995]. From the constitutive relation one can also write

$$\gamma_{1'2'}^{n} = S_{66}^{n}\tau_{1'2'}^{n}, \tag{12}$$

where $S_{66} = 1/G_{12}$. Taking differentials on both sides of Equation (12),

$$d\gamma_{1'2'}^{n} = S_{66}^{n}d\tau_{1'2'}^{n} + dS_{66}^{n}\tau_{1'2'}^{n}. \tag{13}$$

Equation (13) provides an expression for the change in angle $d\phi^n$. This change is added to the fiber angle value of the previous step to obtain the current fiber angle ϕ^n:

$$\phi^n = \phi^{n-1} + d\phi^n. \tag{14}$$

	Length (mm)	Width (mm)	Aspect Ratio
Mesh A	1.00	1.00	1.0
Mesh B	3.00	1.00	3.0
Mesh C	3.00	1.00	3.0

Table 1. Dimensions of the three meshes used in the present analyses.

This angle is used in the current increment, to transform the stresses and the material incremental constitutive matrix computed in the $1'$–$2'$ frame to the 1–2 frame, to return to the solver in ABAQUS. In the absence of damage (or when the damage is small) the angle ϕ^n will be small. But with the accumulation of damage, ϕ^n starts to increase leading to local fiber direction instability. It should be noted that the definition of fiber rotation via Equation (13) allows the possibility of elastic rotation recovery that is instrumental in deformation localization during kink banding.

The steps outlined in this section are repeated at each loading increment until the analyses are completed.

3. Numerical simulations

We assess the capabilities of the present lamina level modeling scheme by simulating the micromechanical analyses performed earlier on unidirectional axially loaded composite lamina [Basu 2005]. This earlier study considered the composite lamina to consist of discretely layered fiber and matrix phases. Fiber elements were assigned linear elastic properties and the matrix elements were modeled as elastic-plastic materials obeying a J2 incremental flow theory of plasticity with a Mises yield criterion and isotropic hardening. Similar FE studies that were performed earlier [Kyriakides et al. 1995; Vogler and Kyriakides 1997; Lee and Waas 1999; Yerramalli and Waas 2004] considered nonuniform fiber spacing effects, 3D effects (variation in fiber packing) and in a limited manner, multiaxial loading. These studies established that a 2D representation of the composite with uniform packing sufficed to capture the important aspects of kink banding, provided that the fiber volume fraction was in excess of 50%.

For this study, the laminae are assumed to be degrading homogenized orthotropic media, with fiber volume fraction of $v_f = 50\%$. Two lamina geometries with aspect ratio AR $= 1$ (1 mm $\times$1 mm dimension) and AR $= 3$ (1 mm $\times$3 mm dimension) are considered (data in Table 1). These laminae are discretized

	Mesh A	Mesh B	Mesh C
Elements	1	3	3600
Nodes	8	18	11041
Degrees of Freedom	16	36	22082

Table 2. Summary of the element and nodal data for mesh A, mesh B and mesh C.

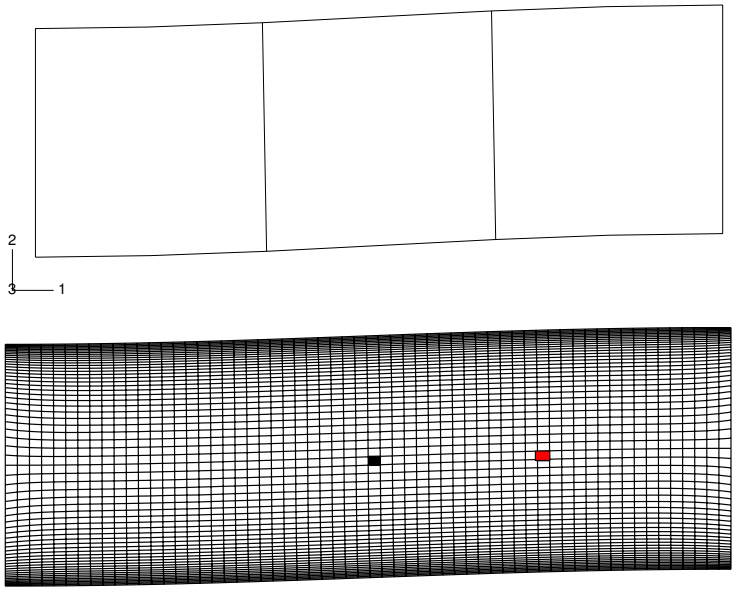

Figure 3. Finite element meshes used in the present analyses for the AR3 lamina. The element darkened at the center is element number 330 and the element shaded in red is element 316. Quantities extracted from these two elements are presented later.

using quadratic plane stress continuum elements CPS8 available in the commercial finite element software package ABAQUS. The AR1 lamina is discretized using a single CPS8 element. The AR3 lamina is meshed using two different finite element discretization schemes which are shown in Figure 3. A summary of the nodal and elemental data are presented in Table 2. In generating these meshes (AR3 mesh) a gradation of element sizes is used, with a finer discretization near the free boundaries. This was done to preclude any artificial stiffening that can be introduced due to edge effects if a uniform mesh is used in conjunction with slight misalignment of the principal material axis with respect to the loading direction. For both ARs, static analyses are performed using displacement control loading. Linear eigenvalue buckling analyses are also performed to generate perturbations in the form of the linear eigen modes to be used in subsequent response analyses. Geometric nonlinearity is included in the response analysis through the RIKS [Riks 1972] option available in ABAQUS.

Elastic material properties for the AS4/3501-6 [Soden et al. 1998] material system are described in Table 3, which are consistent with the lamina properties derived from the fiber and matrix properties described in [Basu 2005]. The nonlinear behavior in shear and in the transverse direction are provided as input, as normalized moduli variation against S_r as shown in Figure 4. A material point is denoted as 'damaged' when S_r at that location reaches S_r^* (or the end of the input stress-strain curve). For this analysis, this refers to a 55% degradation in the in situ secant shear modulus, G_{12}. The complete material constitutive behavior is modeled via the user material subroutine option of ABAQUS. Unit thickness in the z-direction of the lamina is assumed for the plane stress element section definition.

	AS4/3501-6 (GPa)
E_{11}	116.00
E_{22}	12.74
G_{12}	4.78
ν	0.27

Table 3. Elastic constants of the material used in the present study.

Boundary conditions for the laminae are applied at nodal positions and are similar to the micromechanical analyses performed earlier as indicated in Figure 5. The edge AB of the mesh is constrained from moving in the axial or X-direction, but allowed to 'breath' in the transverse or Y-direction. The center point of this edge is prevented from moving at all, eliminating any possible rigid body motion. Edge CD is used to provide the displacement control loading simulating an axial compressive load. Edges AD and BC are allowed to deform as per the equilibrium requirements of the boundary value problem, that is, on these edges $\sigma_{yy} = 0$ and $\tau_{xy} = 0$.

Geometric and material perturbations are both used in the present analyses. Geometric perturbation is provided using the lowermost linear eigenvalue buckling mode such that the perturbed centerline of the mesh creates an angle of 2° with the horizontal at the center of the mesh. In addition, a 2° initial

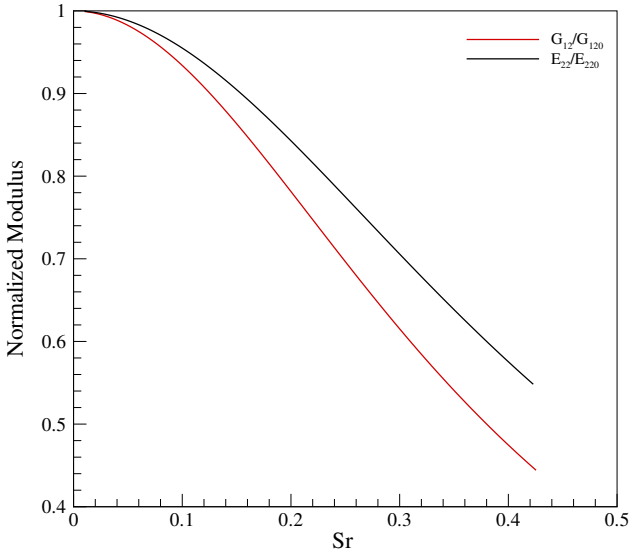

Figure 4. Normalized moduli plotted against the damage parameter S_r.

Figure 5. Boundary conditions and loading used in the present analyses.

fiber angle value (Equation (14)) is used as an initial misalignment. These imperfection magnitudes are similar to the ones used in Basu [2005] and are commonly observed as typical misalignment angles for pre-preg based laminates [Budiansky and Fleck 1993].

4. Results and discussion

Results from the FE study outlined in the previous section are presented here. For each mesh, the load-end shortening data are normalized as described in Equation (15):

$$\sigma = \frac{P}{A}, \qquad \epsilon = \frac{\Delta}{L}. \tag{15}$$

Here, A and L denote the initial cross-sectional area and the initial axial length respectively. Deformed shapes of the finite element mesh at various load levels are presented. Contour plots showing the evolution of the instantaneous fiber rotation angle ϕ and deformation magnitude are also presented.

4.1. ***AR1 lamina results.*** The normalized load-end shortening response ($\bar{\sigma}$-$\bar{\epsilon}$) for the AR1 lamina is shown in Figure 6 with the corresponding result from the micromechanical study [Basu 2005] presented for comparison. The macrolevel response for this aspect ratio matches quite well with the micromechanical prediction. As the mesh A has only 16 degrees of freedom compared to the nearly 128,000 for the micromechanical analysis, it behaves more stiffly than the micromechanical analysis mesh. This is observable in the slight deviation near the peak of the $\bar{\sigma}$-$\bar{\epsilon}$ response of mesh A. On the other hand, such a low resolution of the current mesh does not allow it to capture the gradients of stresses, strains or the deformation field accurately. This actually magnifies the effect of the material imperfection used in the present analysis and we obtain a lower peak load for the AR1 lamina compared to the corresponding micromechanical analysis. The post-peak response from the micromechanical analysis shows a 'snapback' where the stress and the strain both decrease. Subsequently, the response shows a softening behavior where the stress continues to drop with increasing strain. The current analysis follows the peak load with a steep snapback and the stress reaches nearly zero before a softening regime appears in the global response. As mentioned before, the present approach degrades both E_{22} and G_{12}, when $S_r > S_r^*$. This occurs after the global response passes through a peak. As the moduli are degraded, the stresses carried by the system degrade as well. Thus the residual strength and the residual stiffness of the system are both reduced. In the micromechanical analysis, the stresses computed for the matrix elements

remain constant (as the material is modeled as an isotropic hardening material followed by a perfectly plastic regime) which implies a reduction in the effective stiffness. For a lamina, the transverse direction response and the shear response are matrix dominated. Hence the micromechanical analysis produces constant stresses for an equivalent lamina, rather than a degradation in the load carried by it. Thus a softening branch with significant load carrying capacity is observed for the micromechanical analysis which is an artifact of the assumed material model rather than an experimentally observed one. In an experiment, the lamina fails at the peak point rather catastrophically, and the load drops in a near vertical fashion [Oguni et al. 2000].

A sensitivity study is performed to ascertain the effect of the E_{11} degradation beyond $S_r > S_r^*$ on the global response. Figure 7 presents the data from this study and shows the dependence of the post-peak equilibrium path on the rate of degradation of E_{11}. When E_{11} is not degraded, the unstable post-peak equilibrium follows a path nearly parallel to the initial loading path. On the other hand, when E_{11} is degraded by 10% per load increment, the snapback vanishes and the post-peak response assumes a softening behavior. This indicates that there is a rate of E_{11} degradation at which the post-peak response transitions from a snapback to a softening behavior. For this study this rate is nearly 8.5% per load increment and the global response closely resembles observations from laboratory tests [Lee and Waas 1999; Oguni et al. 2000; Yerramalli 2003]. It should be kept in mind that the rate at which the E_{11} degrades is a numerical consideration (to produce a stable algorithm) and does not affect the overall load or the overall behavior. The rates of E_{22} and G_{12} degradations, beyond S_r^*, are fixed at 10% per increment during this study.

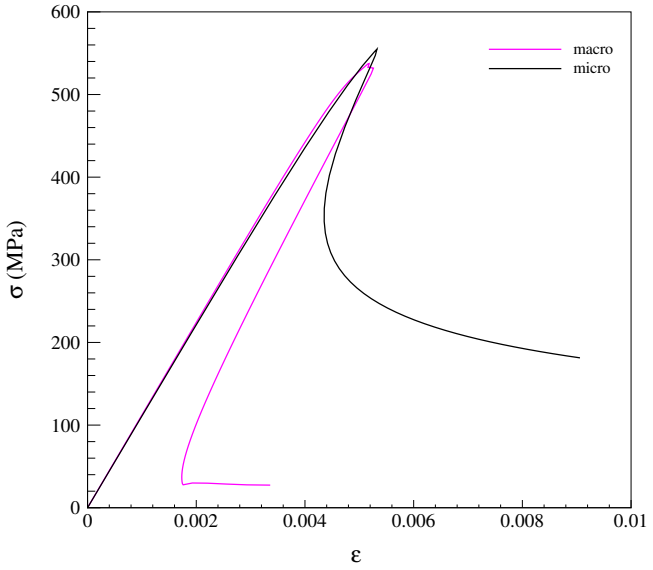

Figure 6. Normalized stress-strain response for AR1 lamina.

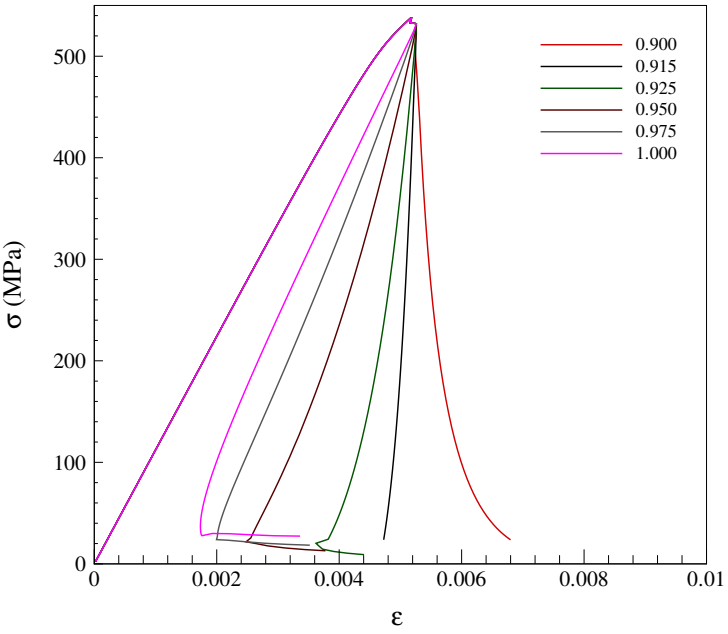

Figure 7. Normalized axial stress-strain response as a function of axial stiffness degradation.

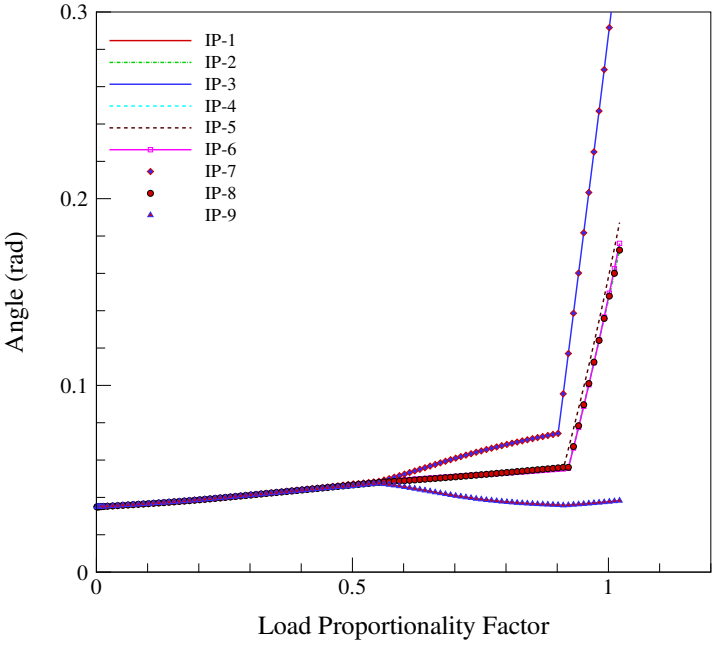

Figure 8. Evolution of instantaneous fiber angle for AR1 lamina.

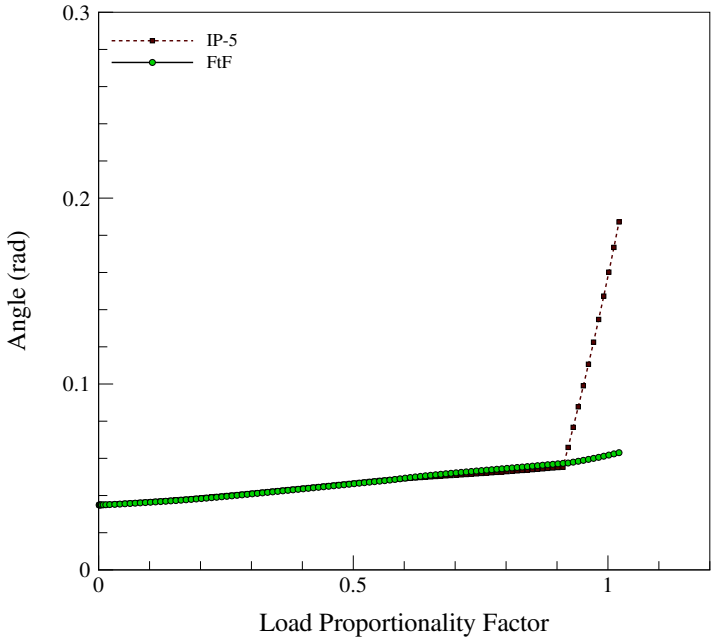

Figure 9. Comparison of instantaneous fiber angle for AR1 geometry computed using two different methods.

Analysis output such as the in situ fiber rotation are also reported for a general E_{11} degradation (5% degradation per load increment) to illustrate the similarities between the present macro-level modeling and the micromechanical analysis. It is understood that this discussion uses the values of different variables sampled at the Gauss points of the CPS8 element in ABAQUS. In situ fiber rotation, ϕ, is plotted in Figure 8. In the prepeak stage, the complete geometry undergoes uniform straining as is evident from the near uniform rotation angle at all locations. Near the peak, the strain distribution becomes nonuniform. While some locations begin to strain faster, some begin to rotate slower than the rest. This phenomenon is similar to the strain redistribution observed during the micromechanical analysis and allows the deformation field to localize and eventually form a kink band. It shall also be noted that, when E_{11} begins to drop in the $S_r > S_r^*$ region, the in situ fiber rotation accelerates, leading to a very large rotation within a small change in loading, precipitating a catastrophic failure event. The results, plotted in Figure 9, show the instantaneous fiber orientation ($1'$-direction) computed using Equation (11) and Equation (14). It can be seen that these two different approaches are nearly identical, which validates the approximations made during derivation of the fiber rotation angle.

4.2. ***AR3 lamina results.*** The normalized load-end shortening response ($\bar{\sigma}$-$\bar{\epsilon}$) of the AR3 lamina are presented in Figure 10. Both mesh B and mesh C capture the overall global behavior though they use widely different finite element discretization. It can be seen that the macro-level responses are stiffer than the micromechanical response, which is because both these meshes have significantly fewer degrees of freedom compared to the micromechanical mesh (less than 10%). Mesh B has the lowest possible

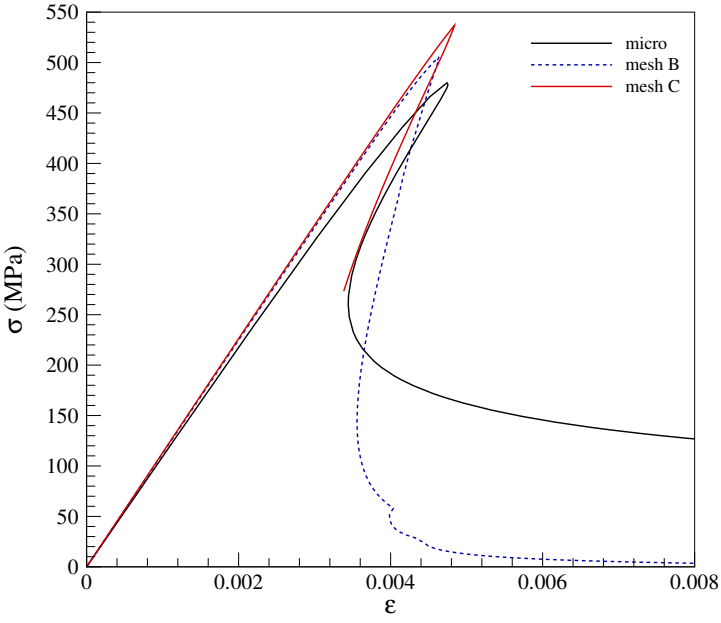

Figure 10. $\bar{\sigma} - \bar{\epsilon}$ response for AR3 lamina.

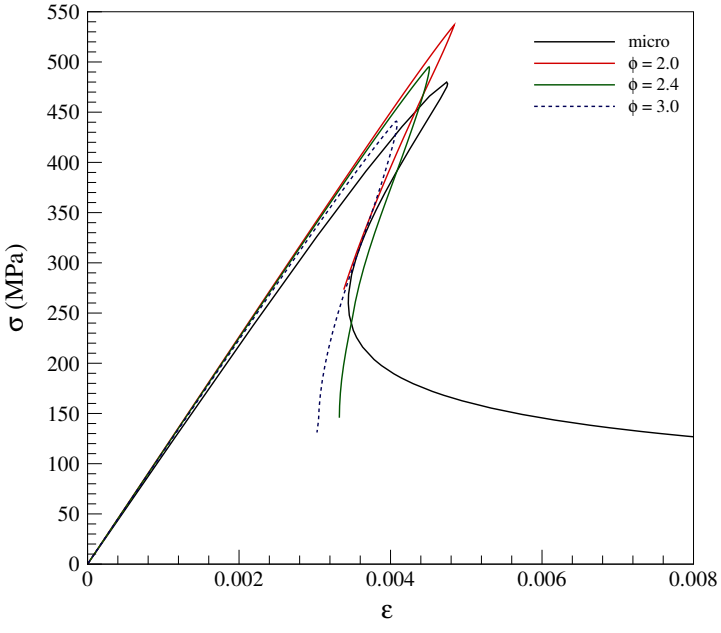

Figure 11. Variation of mesh C response with initial imperfection.

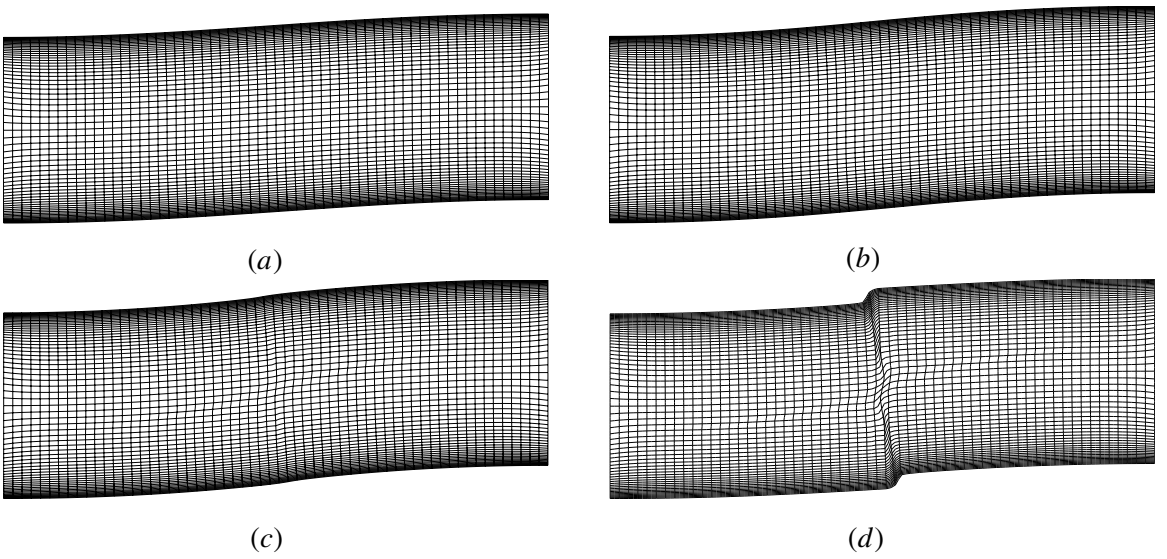

Figure 12. Plots of deformed shape for mesh C at different load levels: (a) 411 MPa, (b) 495 MPa, (c) 420 MPa, (d) 146 MPa.

resolution for this lamina and hence behaves similarly to mesh A. For mesh C, the material imperfection is provided by normalizing the shear strain distribution. Thus an imperfection magnitude of 2° is effectively lower than a uniform 2° imperfection, which appears for mesh B. This is apparent from the peak load predictions of mesh B and mesh C. When the imperfection magnitude of mesh C is increased (effectively bringing the imperfection magnitude closer to the imperfection magnitude of the micromechanical mesh) the peak load matches more closely with the micromechanical prediction as shown in Figure 11.

Plots showing the deformation shapes at various load levels are shown in Figure 12. From these plots it can be observed that a band of elements (four element length wide) at the center of the lamina undergoes severe deformation during the global compression. Using this band as the kink band, the ratio of the kinked and unkinked volumes for this homogenized (or smeared) system is 7% percent compared to the corresponding ratio of 8% percent obtained from the micromechanical analysis.

Colored contour plots showing the distribution of local fiber rotation magnitudes are presented in Figure 14. In the pre-peak region, the complete geometry deforms. As the loading progresses, the fibers rotate locally based on the initial imperfection present in the system. This allows some areas to rotate faster than the rest of the lamina. Locations where fiber rotation is lower store significant amounts of elastic energy. Beyond the peak load, this energy is released and redistributed in the lamina. This results in further rotation of the higher rotation locations leading to a deformation localization which is manifested as a kinked band of fibers. The in situ fiber rotation ϕ is plotted for two different locations on mesh C in Figure 13. This plot reveals that beyond the peak-lead, some portion of the lamina continues straining monotonically whereas some portions release the elastic straining they have undergone. This shows that the elastic strain redistribution which is connected to the stored elastic

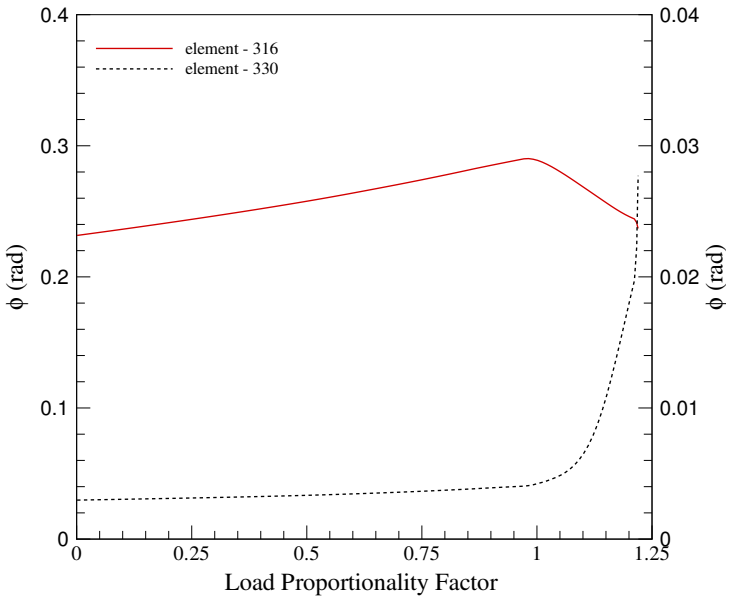

Figure 13. Plot of in situ fiber rotations from two different locations from the mesh C analysis. Element 316 result is plotted on the right-hand side vertical axis. Element 330 result is plotted on the left-hand side vertical axis.

energy causes deformation localization ultimately leading to kink banding. The mechanism of kink banding observed from this macro-level smeared approach is similar to the mechanisms observed in the micromechanical analyses, which validates the analysis approach used here. Thus, it appears that the smeared system, designed to capture the salient features associated with the kink band formation, performs as intended.

Contours of the damage variable S_r are also plotted in Figure 15 for mesh C, which shows the damage accumulation and localization during loading. The areas shaded in gray represent the most damaged regions. It is clear that these contour plots visually capture the region in which deformation is localized. It should be also noted that when the damaged region stretches across the specimen, the load carrying path between the end supports is broken, rendering the specimen unable to carry any more load. In Figure 11, the termination points of the individual responses correspond to this phenomenon.

5. Concluding remarks

In this paper, a mechanism based lamina level modeling approach is developed to study fiber kinking and validated against rigorous micromechanical analyses of unidirectional laminae. This modeling approach uses the complete nonlinear stress-strain relations for the lamina in shear and in transverse tension/compression as input, along with readily available lamina level elastic properties. Using only these (a minimum number) as inputs, compressive failure due to fiber kinking is modeled for unidirectional laminae of varying geometry and varying levels of finite element discretization. The present modeling approach is able to capture the pertinent features of the micromechanical analysis namely, the peak load,

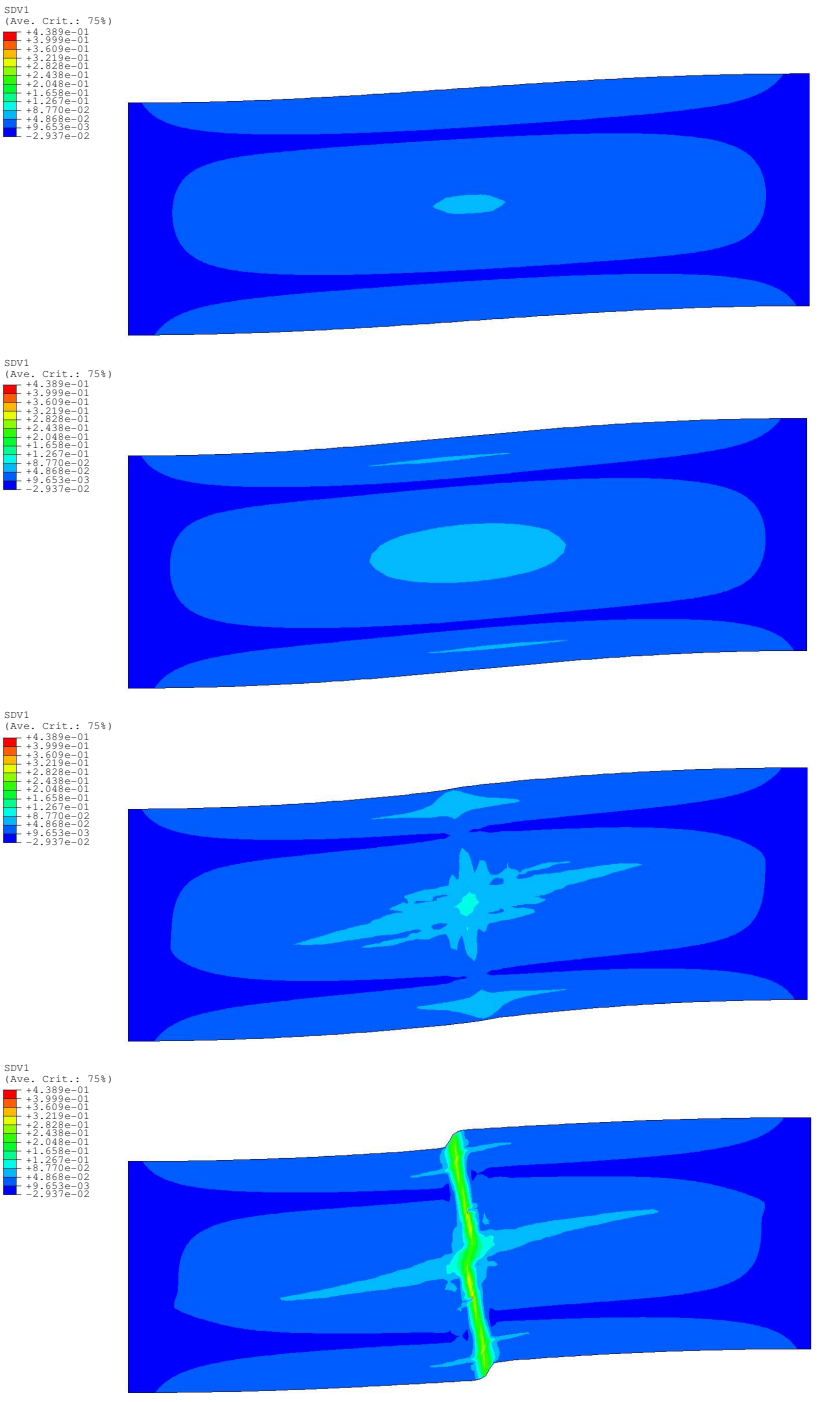

Figure 14. Contour plots showing the in situ fiber angle ϕ at various load levels for mesh C (from top to bottom): 411 MPa, 495 MPa, 420 MPa, 146 MPa.

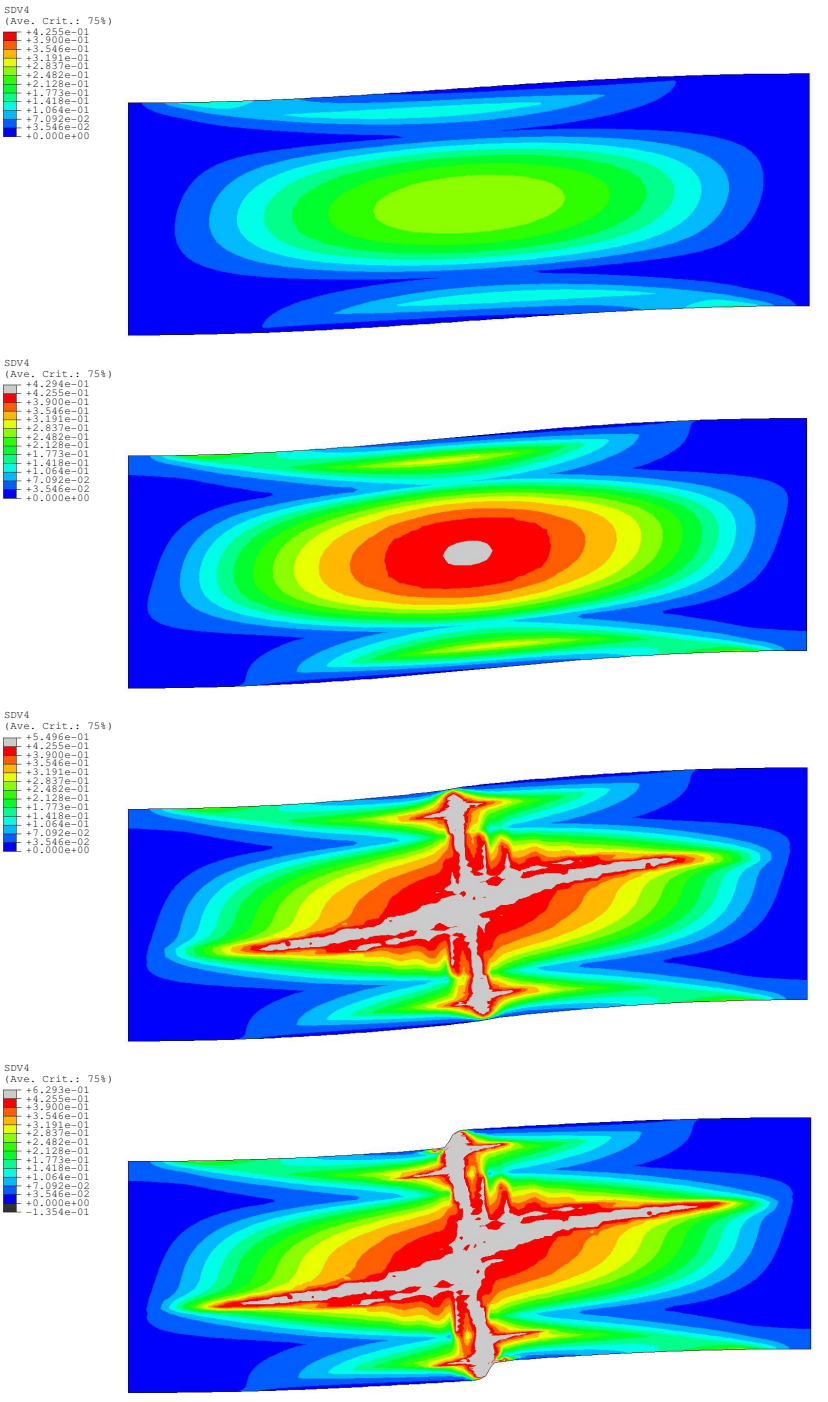

Figure 15. Contour plots showing the damage accumulation from mesh C analysis (from top to bottom): 411 MPa, 495 MPa, 420 MPa, 146 MPa.

the deformation localization and kink band width. Quantitatively the predictions of the present approach matches with the micromechanical analyses very well. The present approach has shown a drastic reduction in the computational costs in capturing a highly nonlinear and complex deformation localization phenomenon. The success of this approach is encouraging and points the way for extending this modeling approach to more complex structural configurations, with increased computational efficiency.

References

[ABAQUS 2003] *ABAQUS user's manual*, Version 6.3-1, Hibbitt and Karlsson and Sorensen Inc., Pawtucket, RI, 2003.

[Basu 2005] S. Basu, *Computational modeling of progressive failure and damage in composite laminates*, Ph.D. thesis, Aerospace Engineering Department, University of Michigan, Ann Arbor, 2005.

[Basu et al. 2006a] S. Basu, A. M. Waas, and D. R. Ambur, "Compressive failure of fiber composites under multiaxial loading", *J. Mech. Phys. Solids* **54**:3 (March 2006), 611–634.

[Basu et al. 2006b] S. Basu, A. M. Waas, and D. R. Ambur, "Prediction of progressive failure in multidirectional composite laminated panels", *Int. J. Solids Struct.* (2006). Available online 18 August 2006.

[Budiansky and Fleck 1993] B. Budiansky and N. A. Fleck, "Compressive failure of fibre composites", *J. Mech. Phys. Solids* **41**:1 (1993), 183–211.

[Chang and Lessard 1991] F.-K. Chang and L. B. Lessard, "Damage tolerance of laminated composites containing an open hole and subjected to compressive loadings: part I–analysis", *J. Compos. Mater.* **25** (January 1991), 2–43.

[Dávila et al. 2000] C. G. Dávila, D. R. Ambur, and D. M. McGowan, "Analytical prediction of damage growth in notched composite panels loaded in compression", *J. Aircr.* **37**:5 (2000), 898–905.

[Evans and Adler 1978] A. G. Evans and W. F. Adler, "Kinking as a mode of structural degradation in carbon fiber composites", *Acta Metall.* **26** (1978), 725–738.

[Fu and Zhang 2006] Y. B. Fu and Y. T. Zhang, "Continuum-mechanical modelling of kink-band formation in fibre-reinforced composites", *Int. J. Solids Struct.* **43**:11–12 (2006), 3306–3323.

[Fung and Tong 2001] Y. C. Fung and P. Tong, *Classical and computational solid mechanics*, World Scientific, Singapore, 2001.

[Goyal et al. 2002] V. K. Goyal, N. Jaunky, E. R. Johnson, and D. Ambur, "Intralaminar and interlaminar progressive failure analysis of composite panels with circular cutouts", pp. 1–12 in *43rd SDM Conference* (AIAA 2002-1745) (Denver, 2002), AIAA, 2002.

[Hashin 1980] Z. Hashin, "Failure criteria for unidirectional fiber composites", *J. Appl. Mech.* (*Trans. ASME*) **47** (June 1980), 329–334.

[Kyriakides et al. 1995] S. Kyriakides, R. Arseculeratne, E. J. Perry, and K. M. Liechti, "On the compressive failure of fiber reinforced composites", *Int. J. Solids Struct.* **32**:6/7 (1995), 689–738.

[Lee and Waas 1999] S. H. Lee and A. M. Waas, "Compressive response and failure of fiber reinforced unidirectional composites", *Int. J. Fract.* **100**:3 (1999), 275–306.

[Merodio and Pence 2001] J. Merodio and T. J. Pence, "Kink surfaces in a directionally reinforced neo-Hookean material under plane deformation, II: Kink band stability and maximally dissipative band broadening", *J. Elasticity* **62**:2 (2001), 145–170.

[Oguni et al. 2000] K. Oguni, C. Y. Tan, and G. Ravichandran, "Failure mode transition in unidirectional E-glass/vinylester composites under multiaxial compression", *J. Compos. Mater.* **34**:24 (2000), 2081–2097.

[Riks 1972] E. Riks, "The application of Newton's method to the problem of elastic stability", *J. Appl. Mech.* (*Trans. ASME*) **39**:4 (1972), 1060–1065.

[Schapery 1989] R. A. Schapery, "Mechanical characterization and analysis of inelastic composite laminates with growing damage", *Mech. Compos. Mater. Struct.* **AMD-100** (1989), 1–9.

[Schapery 1990] R. A. Schapery, "A theory of mechanical behavior of elastic media with growing damage and other changes in structure", *J. Mech. Phys. Solids* **38**:2 (1990), 215–253.

[Schapery 1995] R. A. Schapery, "Prediction of compressive strength and kink bands in composites using a work potential", *Int. J. Solids Struct.* **32**:6/7 (1995), 739–765.

[Schapery 2002] R. A. Schapery, Private communication, 2002.

[Schapery and Sicking 1995] R. A. Schapery and D. L. Sicking, "On nonlinear constitutive equations for elastic and viscoelastic composites with growing damage", pp. 45–76 in *Proceedings of the Seventh International Conference on Mechanical Behavior of Materials*, Society of Materials Science, Kyoto, 1995.

[Soden et al. 1998] P. Soden, M. J. Hinton, and A. S. Kaddour, "Lamina properties, lay-up configurations and loading conditions for a range of fibre-reinforced composite laminates", *Compos. Sci. Technol.* **58**:7 (1998), 1011–1022.

[Sun and Chen 1989] C. T. Sun and J. L. Chen, "A simple flow rule for characterizing nonlinear behavior of fiber composites", *J. Compos. Mater.* **23**:10 (October 1989), 1009–1020.

[Vogler and Kyriakides 1997] T. J. Vogler and S. Kyriakides, "Initiation and axial propagation of kink bands in fiber composites", *Acta Mater.* **45**:6 (1997), 2443–2454.

[Vogler and Kyriakides 1999] T. J. Vogler and S. Kyriakides, "On the axial propagation of kink bands in fiber composites: part I experiments", *Int. J. Solids Struct.* **36**:4 (1999), 557–574.

[Yerramalli 2003] C. Yerramalli, *A mechanism based Modeling approach to failure in fiber reinforced composites*, Ph.D. thesis, Aerospace Engineering Department, University of Michigan, Ann Arbor, 2003.

[Yerramalli and Waas 2004] C. S. Yerramalli and A. M. Waas, "The effect of fiber diameter on the compressive strength of composites; A 3D finite element based study", *Comput. Model. Eng. Sci.* **6**:1 (2004), 1–16.

Received 8 Dec 2005.

SHILADITYA BASU: basus@umich.edu
Technical Professional–Marine, Granherne Inc., 601 Jefferson Ave., Houston, TX 77054, United States

ANTHONY M. WAAS: dcw@umich.edu
Composite Structures Laboratory, Aerospace Engineering Department, University of Michigan, 1320 Beal Avenue, Ann Arbor, MI 48109, United States

DAMODAR R. AMBUR: damodar.r.ambur@nasa.gov
Structures Division, NASA Glenn Research Center, Cleveland, OH 44135, United States